could be used with new estimates of the suppression parameter to yield appreciably larger estimates of the hydrogen content in the shallow lunar subsurface.

17. D. A. Paige *et al.*, *Science* **330**, 479 (2010).
18. J. R. Salvail, F. P. Fanale, *Icarus* **111**, 441 (1994).
19. A. R. Vasavada, D. A. Paige, S. E. Wood, *Icarus* **141**, 179 (1999).
20. W. V. Boynton *et al.*, *Science* **297**, 81 (2002).
21. I. Mitrofanov *et al.*, *Science* **297**, 78 (2002).
22. D. H. Crider, R. R. Vondrak, *J. Geophys. Res.* **108**, 5079 (2003).
23. D. H. Crider, R. R. Vondrak, *Adv. Space Res.* **31**, 2293 (2003).
24. The LRO Mission is supported by the NASA Exploration System Mission Directorate, and the LEND investigation is supported by the Russian Federal Space Agency. We acknowledge the LRO Project team at NASA's Goddard Space Flight Center for their outstanding support of the LEND investigation.

A New Mixing Diagnostic and Gulf Oil Spill Movement

Igor Mezić,[1]* S. Loire,[1]† Vladimir A. Fonoberov,[2]† P. Hogan[3]

Chaotic advection has served as the paradigm for mixing in fluid flows with simple time dependence. Its skeletal structure is based on analysis of invariant attracting and repelling manifolds in fluid flows. Here we develop a finite-time theory for two-dimensional incompressible fluid flows with arbitrary time dependence and introduce a new mixing diagnostic based on it. Besides stretching events around attracting and repelling manifolds, this allows us to detect hyperbolic mixing zones. We used the new diagnostic to forecast the spatial location and timing of oil washing ashore in Plaquemines Parish and Grand Isle, Louisiana, and Pensacola, Florida, in May 2010 and the flow of oil toward Panama City Beach, Florida, in June 2010.

Chaotic advection theory (*1–3*) explains the phenomenon of mixing behavior in fluid flows with simple time dependence. This is achieved using hyperbolicity concepts associated with attracting and repelling lines, as well as hyperbolic zones with strongly chaotic behavior (*4*). However, chaotic advection and mixing phenomenology in that case depend on the recurrence of hyperbolic behavior and thus are difficult to extend to analyze flows with complex time dependence, such as those occurring in the ocean and atmosphere. Detecting geometric structures has become increasingly important in analyzing fluid flows with complex time dependence because of the realization that even turbulent flows feature Lagrangian structures that can be understood from the perspective of finite-time dynamical systems theory (*5–7*). This has led to the development of the theory of Lagrangian coherent structures (*8*), within which researchers focused on finite-time behavior, such as finding the attracting or repelling finite-time invariant curves (*5, 6, 9, 10*). In (*11*), an alternative approach stems from studies of the statistical properties of dynamical systems, showing that Lagrangian time-averages of physically relevant functions on state space enable the detection of invariant sets of dynamical systems, including experimentally realizable fluid flows with simple time dependence (*12–14*). Here we develop this theory further, based on the gradient of the average Lagrangian velocity field.

[1]Center for Control, Dynamical Systems and Computation, and Department of Mechanical Engineering, University of California, Santa Barbara, CA 93106, USA. [2]Aimdyn, Santa Barbara, CA 93101, USA. [3]Naval Research Laboratory, Stennis Space Center, MS 39529, USA.

*To whom correspondence should be addressed. E-mail: mezic@engineering.ucsb.edu
†These authors contributed equally to this work.

Consider the time evolution of a fluid flow on time interval $\tau = [t_0, t_0 + T]$. The dynamics of fluid particles in an incompressible two-dimensional (2D) flow on a domain $A \subset R^2$ is given by

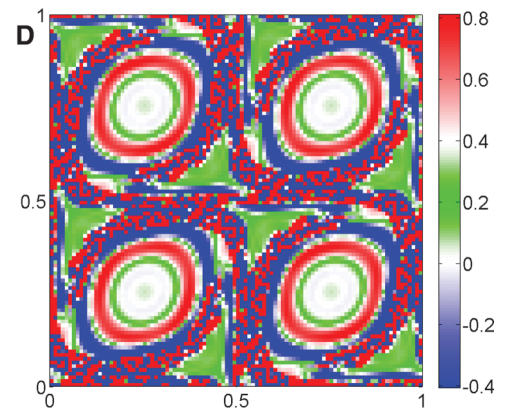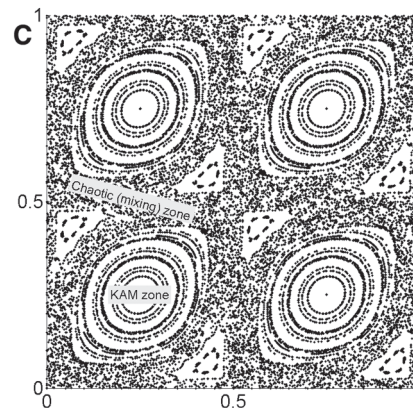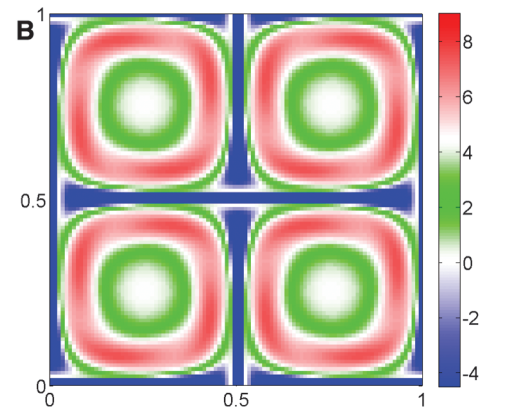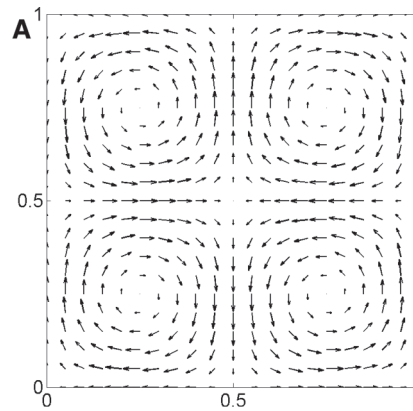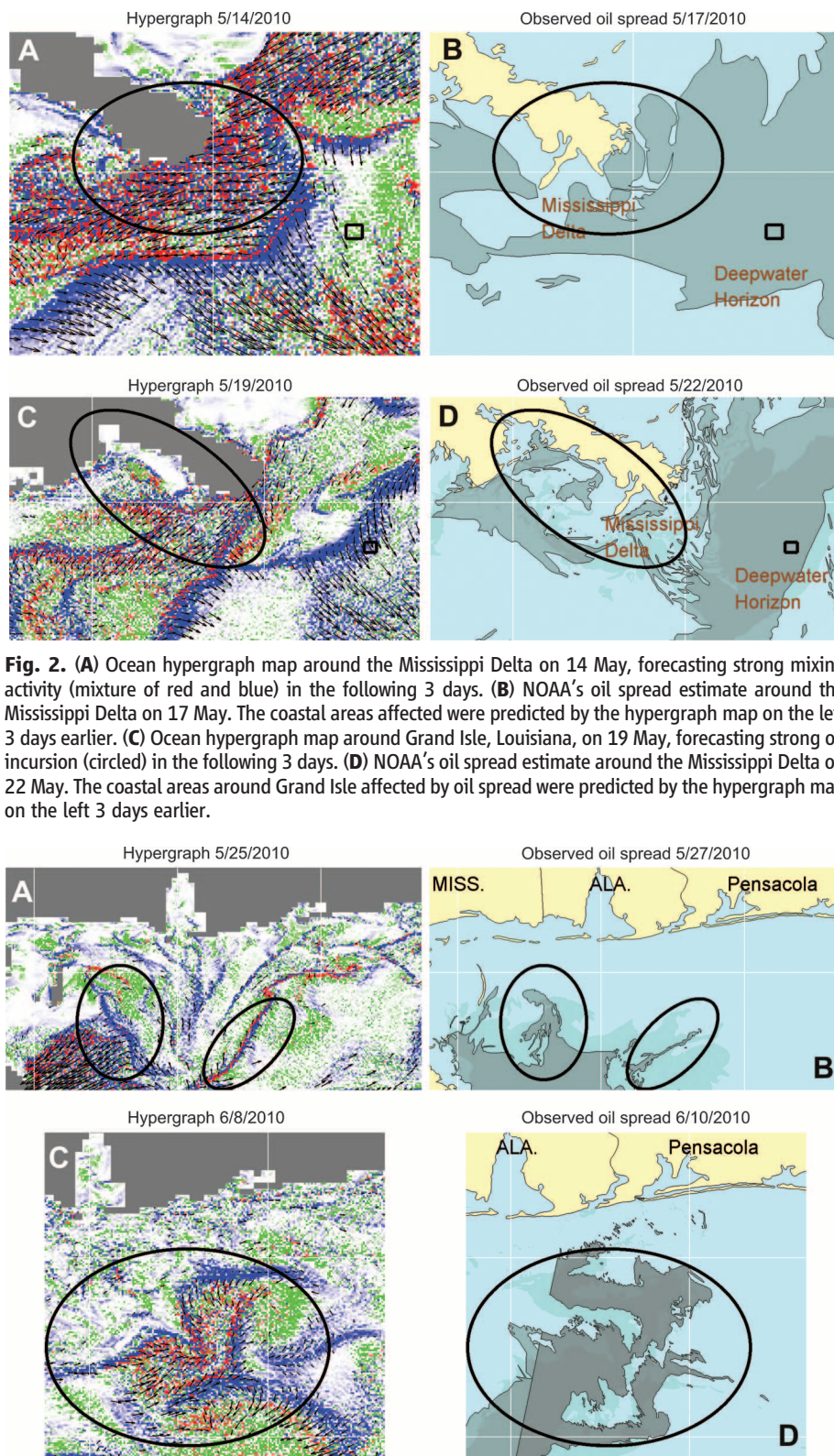$$\dot{\mathbf{x}} = \mathbf{v}(\mathbf{x}, t) \qquad (1)$$

where $\nabla \cdot \mathbf{v} = 0$. The position of the fluid particle starting at time t_0 at a cartesian spatial location $\mathbf{x}_0 = (x_0, y_0)$ moves to $(x(t_0 + T, x_0, y_0, t_0), y(t_0 + T, x_0, y_0, t_0))$ at time $t_0 + T$

$$x(t_0 + T, x_0, y_0, t_0) = x_0 + \int_{t_0}^{t_0+T} v_x(t, x(t_0 + t, x_0, y_0, t_0), y(t_0 + t, x_0, y_0, t_0)) dt \qquad (2)$$

$$y(t_0 + T, x_0, y_0, t_0) = y_0 + \int_{t_0}^{t_0+T} v_y(t, x(t_0 + t, x_0, y_0, t_0), y(t_0 + t, x_0, y_0, t_0)) dt \qquad (3)$$

If we denote by $\mathbf{v}^*(\mathbf{x}_0, t_0, T) = (v_x^*(x_0, y_0, t_0, T), v_y^*(x_0, y_0, t_0, T))$ the average Lagrangian velocity on τ starting from $\mathbf{x}_0$, we have

$$x(t_0 + T, x_0, y_0, t_0) = x_0 + T v_x^*(x_0, y_0, t_0, T) \quad (4)$$

$$y(t_0 + T, x_0, y_0, t_0) = y_0 + T v_y^*(x_0, y_0, t_0, T) \quad (5)$$

Fig. 1. (**A**) A cellular, divergence-free velocity field described in Eq. 6. (**B**) Hypergraph map for the velocity field shown in (A), for $T = 0.94248$. (**C**) Poincaré map for the time-periodic, divergence-free perturbation of the velocity field shown in (A) by a vector field described in Eq. 7, with $\varepsilon = 0.1$. (**D**) Hypergraph map for the time-periodic velocity field whose Poincaré map is shown in (C), for $T = \pi$.

Fig. 2. (**A**) Ocean hypergraph map around the Mississippi Delta on 14 May, forecasting strong mixing activity (mixture of red and blue) in the following 3 days. (**B**) NOAA's oil spread estimate around the Mississippi Delta on 17 May. The coastal areas affected were predicted by the hypergraph map on the left 3 days earlier. (**C**) Ocean hypergraph map around Grand Isle, Louisiana, on 19 May, forecasting strong oil incursion (circled) in the following 3 days. (**D**) NOAA's oil spread estimate around the Mississippi Delta on 22 May. The coastal areas around Grand Isle affected by oil spread were predicted by the hypergraph map on the left 3 days earlier.
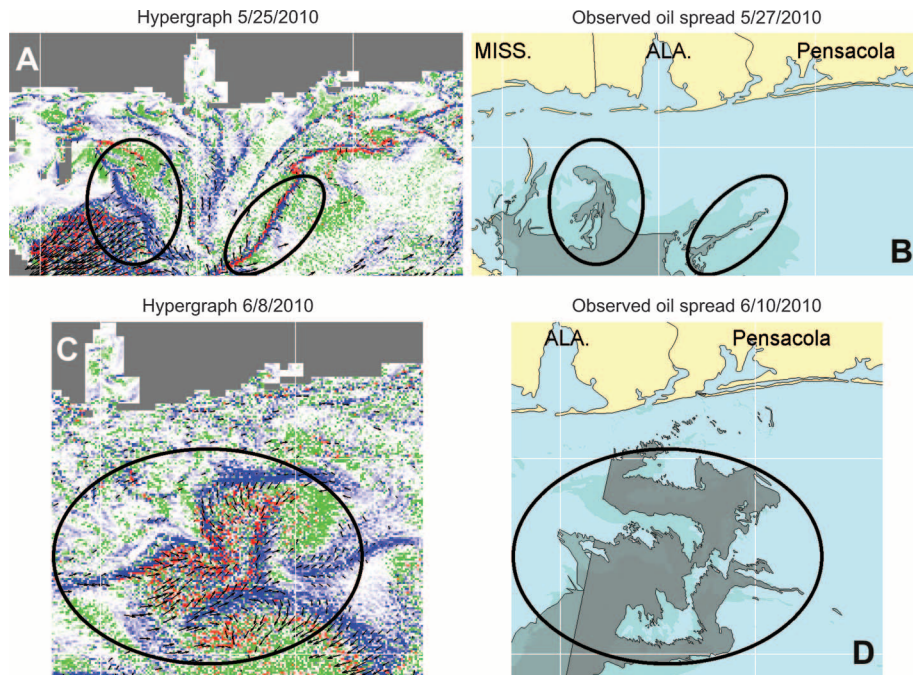

Fig. 3. (**A**) Ocean hypergraph map in front of the Biloxi-Pensacola shoreline on 25 May, forecasting strong oil incursion toward the coastline (circled) in the following 3 days. (**B**) NOAA's oil spread estimate in front of the Biloxi-Pensacola shoreline on 27 May. The major directions of oil spread were predicted by the hypergraph map 2 days earlier. The oil reached the shore several days later, on 2 June. (**C**) Ocean hypergraph map in front of Pensacola on 8 June, forecasting a strong oil mixing event in front of the shoreline and extension of the oil slick toward Panama City Beach in the following 3 days. (**D**) NOAA's oil spread estimate on 10 June in front of Pensacola. The oil developed a large slick forecasted by the hypergraph map 2 days earlier and continued to flow toward Panama City Beach.

We call $\mathbf{v}^*(\mathbf{x}_0, t_0, T)$ the mesochronic velocity field (15).

We denote by $\phi_{t_0}^{t+T}(\mathbf{x}_0)$ as the map of A mapping the fluid particle starting at time t_0 at point $\mathbf{x}_0 \in R^2$ to its position $\mathbf{x}$ at time $t_0 + T$. This map represents the solution of Eq. 1. Its derivative $D\phi_{t_0}^{t+T}(\mathbf{x}_0)$ is the Jacobian matrix $J(\mathbf{x}_0) = \partial\mathbf{x}/\partial\mathbf{x}_0$. Because $\mathbf{v}$ is divergence-free, the eigenvalues $\lambda_{1,2}(\mathbf{x}_0)$ of $J(\mathbf{x}_0)$ satisfy $\det(J(\mathbf{x}_0)) = \lambda_1(\mathbf{x}_0)\lambda_2(\mathbf{x}_0) = 1$. Thus, they are either real with $\lambda_1(\mathbf{x}_0) = 1/\lambda_2(\mathbf{x}_0)$ or complex-conjugate on the unit circle, $|\lambda_{1,2}(\mathbf{x}_0)| = 1$. We call a trajectory starting at $\mathbf{x}_0$ mesohyperbolic (hyperbolic on average) if $\lambda_{1,2}(\mathbf{x}_0)$ are real and different from 1, and mesoelliptic (elliptic on average) if the eigenvalues are complex-conjugate.

The calculation shown in (4) now leads to the conclusion that a trajectory starting at $\mathbf{x}_0$ is mesohyperbolic on τ, provided that $\det\nabla\mathbf{v}^*(\mathbf{x}_0) < 0$ or $\det\nabla\mathbf{v}^*(\mathbf{x}_0) > 4/T^2$, whereas it is mesoelliptic, provided that $0 < \det\nabla\mathbf{v}^*(\mathbf{x}_0) < 4/T^2$. There are also differences in behavior between the case $\det\nabla\mathbf{v}^*(\mathbf{x}_0) < 0$ or $\det\nabla\mathbf{v}^*(\mathbf{x}_0) > 4/T^2$. The local, linearized map behavior in the case $\det\nabla\mathbf{v}^*(\mathbf{x}_0) < 0$ is a pure strain (fig. S4A), whereas in the case of d $\det\nabla\mathbf{v}^*(\mathbf{x}_0) > 4/T^2$, it is strain combined with a 180° rotation (that is, reflection across the x and y axes) (fig. S4B). When T goes to zero, the mesohyperbolicity/mesoellipticity criterion goes to the well-known Okubo-Weiss criterion (16, 17) for instantaneous snapshots of time-dependent velocity fields, where a region is called elliptic provided that $\det\nabla\mathbf{v} > 0$ in that region and hyperbolic in the region where $\det\nabla\mathbf{v} < 0$.

The Lagrangian coherent structures theory is based on the calculation of the ridges of the finite-time Lyapunov exponent (FTLE) field (7, 18, 19). In contrast to the theory of Lagrangian coherent structures that determines the stretching skeleton of a fluid flow depending on the extrema of the FTLE field [or the extrema of $\det\nabla\mathbf{v}(\mathbf{x}_0, t, t_0)$ over a time interval $[t_0, t]$ (20)], our approach is putting emphasis on the average behavior of trajectories over an interval of time. In contrast to the FTLE method, the mesohyperbolicity calculation distinguishes between two different regions of hyperbolic behavior (which we show in examples below enables characterization of mixing regions) and provides the ability for gradation of the elliptic regions. For more detailed comparison, see (4).

Although the field we use to distinguish kinematically separate regions is not frame-invariant, it can be improved to account for the rate of rotation of the strain along the lines pursued in (21, 22).

The field $\det\nabla\mathbf{v}^*(\mathbf{x}_0)$ becomes the centerpiece of our finite-time diagnostics of the Lagrangian properties. To build intuition, we begin with a simple, well-understood, cellular velocity field shown in Fig. 1A, described by

$$\mathbf{u}(\mathbf{x}) = \begin{bmatrix} -\sin(2\pi x_1)\cos(2\pi x_2) \\ \cos(2\pi x_1)\sin(2\pi x_2) \end{bmatrix} \quad (6)$$

This divergence-free flow has families of periodic orbits around elliptic fixed points bounded by heteroclinic orbits that connect hyperbolic

(saddle) points. In Fig. 1B, we show the $\det\nabla\mathbf{v}^*$ field for the velocity field in Fig. 1A, computed for $T = 0.94248$. The color scheme is as follows: blue indicates regions of $\det\nabla\mathbf{v}^* < 0$ (mesohyperbolic with pure strain); white and green indicate $0 \leq \det\nabla\mathbf{v}^* \leq 4/T^2$; and red indicates $4/T^2 < \det\nabla\mathbf{v}^*$ (mesohyperbolic with strain and 180° rotation). As expected, the areas around the elliptic fixed points inside the cells are white (because the period of calculation is close to the period of the linear rotation around the elliptic fixed point, over time T, particles close to the elliptic fixed point make one full circle, and their rotation angle is close to zero) and green, indicating mesoelliptic behavior there. There is a red ring of hyperbolic behavior inside the cell, due to finite-time strain and 180° rotation (this feature is also observed inside the eddies produced by the model of ocean flow in the Gulf of Mexico). The area around heteroclinic orbits is blue, indicating pure strain behavior. Thus, in this integrable case, the $\det\nabla\mathbf{v}^*$ field represents the known properties of the dynamics well.

Next, we analyze the same base field $\mathbf{u}$ perturbed by a time-dependent perturbation velocity

$$\mathbf{u}_p(\mathbf{x}) = \varepsilon \cdot \cos(2\pi t)$$
$$\times \begin{bmatrix} -\sin(2\pi(x_1 - 0.25))\cos(2\pi(x_2 - 0.25)) \\ \cos(2\pi(x_1 - 0.25))\sin(2\pi(x_2 - 0.25)) \end{bmatrix} \quad (7)$$

where $\mathbf{x} = (x_1, x_2)$, $\varepsilon = 0.1$. This velocity field is time-periodic, with period 1. The standard way to visualize such systems is the Poincaré map method. The Poincaré map for the time-periodically perturbed cellular velocity field is shown in Fig. 1C. This Poincaré map shows the well-understood mixture of chaotic behavior, as indicated by orbits filling an area of the phase space, and Kolmogorov-Arnold-Moser (KAM) orbits, surrounding elliptic fixed points and elliptic periodic orbits. In Fig. 1D we show the associated $\det\nabla\mathbf{v}^*$ field, for time interval $T = \pi$. The white and green zones are positioned in the same general area where KAM curves are present. The red ring inside the KAM zone, indicating finite-time strain with 180° rotation, appears in the time-dependent flow as well. The mixing zones in the Poincaré map plot are indicated by the mixture (pure strain plus strain with 180° rotation) of the mesohyperbolic behavior, as indicated by the mixture of red and blue at those mixing locations in Fig. 1D. The feature of chaotic dynamics that we observed for the simple time-periodic cellular flow, producing a mixture of pure strain and strain plus 180° rotation in the zones of intersection of stable and unstable manifolds, has not been observed before and is interesting in its own right. We will call the plot of the field $\det\nabla\mathbf{v}^*$ the hypergraph map.

As an example of this approach, we computed mesohyperbolicity in a numerical model of the Gulf of Mexico. The model has been configured with the Hybrid Coordinate Ocean Model (HYCOM) with 1/25° horizontal resolution and 20 layers in the vertical. Lateral boundary conditions are taken from a 1/12° HYCOM Atlantic model. The Gulf of Mexico system assimilates satellite sea surface height (SSH) and sea surface temperature (SST) observations and runs in near real-time. The Navy Coupled Ocean Data Assimilation (NCODA) system is used for quality control and data assimilation, which includes in situ profile assimilation in addition to the surface observations. Surface wind and heat flux forcing are provided by the 0.5° NOGAPS product. The model was initialized on 2 September 2003 and continues to the present day.

Model analysis and forecasts are compared to independent (nonassimilated) infrared frontal positions and drifter trajectories. The system shows substantial ability to simulate the major circulation features of the Gulf of Mexico, including the Loop Current Extension and associated Loop Current Eddy shedding. Cyclonic shingle eddies are also accurately simulated. The system produces a 5-day forecast that contains information about hourly velocities, temperature, and salinity.

The hypergraph map is computed for a 3-day time interval starting at 0 hours [details of the computation and the model are given in (4)], using surface velocities produced by the HYCOM model. Consideration of the full physical problem would require a 3D, steady source computation of oil spill, where oil is subject to weathering and chemical reactions in the ocean. To simplify the problem, in our calculations we did not account for the differential motion between the ocean stream and the (possibly 1-μm-thick layer of) oil; that is, we treated oil as a passive scalar moved by the ocean surface velocity or alternatively as indestructible Lagrangian particles. In addition, 3D effects were neglected. These are important near shore, but commonly enhance intense 2D mixing events (23), and thus one can view our 2D mixing predictions as an underestimate of the 3D case. The oil spill is a steady source process, whose theoretical description has received attention (24, 25), but we pursued the problem of surface transport of oil that leaked several days earlier. Thus, the constant replenishment, although important if the full problem of the oil spill is modeled, does not affect our conclusions.

Figures 2 and 3 show a sequence of hypergraph maps corresponding to the Gulf of Mexico–HYCOM model of the Gulf of Mexico surface velocity fields calculated on 14, 19, and 25 May and 8 June as compared with the estimated spread of oil several days after the hypergraph map information. We start with the estimated boundary of the oil spill at the date when the hypergraph map is calculated for the future 3 days. Isolated, elongated red and blue streaks that intersect the oil slick boundary indicate likely advancement directions of the oil slick. The oil is expected to flow in that direction, form a convergence line, and develop filaments. Diffuse zones of red and blue mixture indicate possible mixing events. Such events produce the extension of oil slicks to these zones within several days. We present several such stretching and mixing events and compare those qualitatively with available data on the oil slick extent. The oil extent was estimated by the National Oceanic and Atmospheric Administration (NOAA) (26) and is also available at the *New York Times* Web site (27).

The hypergraph map for 14 May 2010 around the Mississippi Delta (Fig. 2A) forecasted strong mixing activity (mixture of red and blue) in the

Fig. 4. (A) The hypergraph map for the full Gulf of Mexico, showing mesohyperbolic and mesoelliptic regions on 25 June 2010. This map is characteristic of the maps we computed over the 40 days of (from 10 May to 1 July 2010). **(B)** Zoom of the map shown in (A), showing another strong mixing event around Plaquemines Parish, Louisiana.
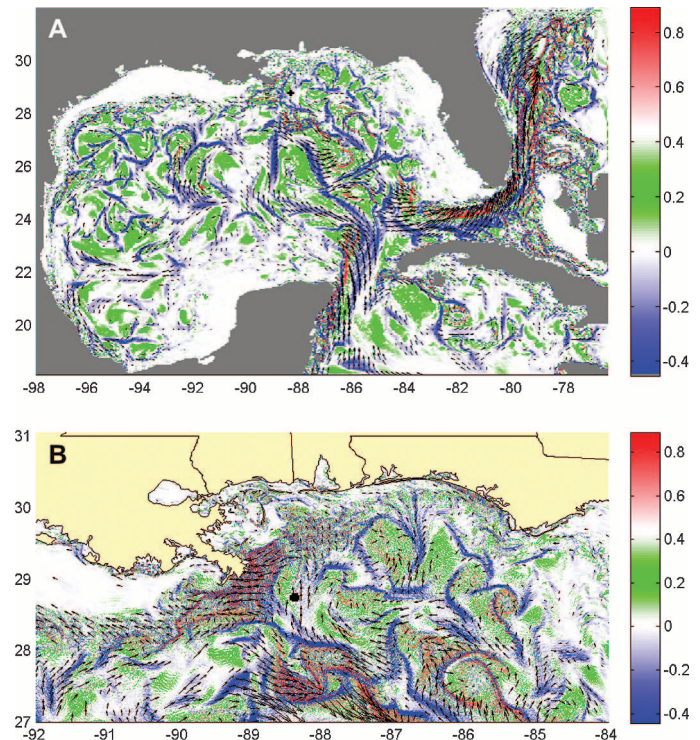
following 3 days. Figure 2B shows that such strong mixing events occurred, 3 days later around the Mississippi Delta and elsewhere in Plaquemines Parish, Louisiana (27). Mixing events around the Mississippi Delta continued to occur on a regular basis.

The hypergraph map (Fig. 2C) on 19 May 2010 forecasted oil incursion in the following 3 days, as was seen on Grand Isle on 22 May (Fig. 2D). The filaments seen in the data (Fig. 2D) are close to blue and red streaks in the hypergraph map (Fig. 2C).

On 25 May (Fig. 3A), the hypergraph map forecasted strong oil incursion toward the coastline between Biloxi, Mississippi, and Pensacola, Florida, in the following 3 days, along the circled convergence lines shown in red and blue. Based on this, we expected that filaments of the oil spill would extend in these directions. Such filaments were seen on 27 May (Fig. 3B). These major directions of oil spread were predicted by the hypergraph map 2 days earlier. The oil reached the shore on 2 June (27).

On 8 June 2010, the hypergraph map forecasted a strong oil mixing event (Fig. 3C), as evidenced by the mixture of red and blue in the circled area, in front of the shoreline and the extension of the oil slick toward Panama City Beach, Florida, in the following days. On 10 June 2010, a large slick developed in the area of the mixing event featured in the hypergraph map 2 days earlier, and it continued to flow toward Panama City Beach (Fig. 3D).

Based on the simulation for the full Gulf of Mexico region (Fig. 4A; the extent is typical for the situation on other dates), we estimated that the spill, if it continued, would eventually reach 80% of the Gulf of Mexico. This is an indication of what a future spill might cause if it is not contained rapidly and does not evaporate quickly. The zoom in Fig. 4B shows the situation close to the oil spill location area around Plaquemines Parish, which continued to show strong mixing activity.

Surface currents, 3-day average Lagrangian velocities, and hypergraph maps for the period from 10 May to 1 July 2010, for the full Gulf of Mexico, and the zoom for the region around the Deepwater Horizon spill, are animated in movies S1 to S6 (4).

There are many physical processes that control the fragmentation of the oil slick on the surface, including Langmuir circulations, that are not captured by the HYCOM model. However, the complexity of the arrangement of mesohyperbolic regions (Fig. 4A) seems to control the stretching and mixing events at large scales. This helps in understanding the fragmentation of oil slicks on the surface of the Gulf of Mexico featured in numerous satellite images and aerial photographs.

One use of these sorts of computations is in oil containment and cleanup. The mesohyperbolicity calculations can provide detailed spatial locations of mixing and concentration events days in advance. In addition, if a layer model is used, providing the velocity field at different depths,

information on possible locations of underwater plumes can be uncovered and supplied to research vessels so they can perform detailed measurements at those locations.

References and Notes

1. H. Aref, *J. Fluid Mech.* **192**, 115 (1984).
2. J. Ottino, *The Kinematics of Mixing: Stretching, Chaos and Transport* (Cambridge Univ. Press, Cambridge, 1989).
3. S. Wiggins, *Chaotic Transport in Dynamical Systems* (Springer-Verlag, New York, Heidelberg, Berlin, 1992).
4. Materials and methods are available as supporting material on *Science* Online.
5. G. Haller, A. Poje, *Phys. D* **119**, 352 (1998).
6. G. Haller, *Phys. Fluids* **13**, 3365 (2001).
7. S. Shadden, F. Lekien, J. Marsden, *Phys. D* **212**, 271 (2005).
8. G. Haller, G. Yuan, *Phys. D* **147**, 352 (2000).
9. F. Lekien, S. Shadden, J. Marsden, *J. Math. Phys.* **48**, 065404 (2007).
10. A. Berger, T. Doan, S. Siegmund, *Discrete Continuous Dyn. Syst. Ser. B* **9**, 3 (2008).
11. A. Poje, G. Haller, I. Mezić, *Phys. Fluids* **11**, 2963 (1999).
12. I. Mezic, S. Wiggins, *J. Nonlinear Sci.* **9**, 213 (1999).
13. N. Malhotra, I. Mezic, S. Wiggins, *Int. J. Bifurcat. Chaos* **8**, 1053 (1998).
14. I. Mezić, F. Sotiropoulos, *Phys. Fluids* **14**, 2235 (2002).
15. Z. Levnajić, I. Mezić, *Chaos* **20**, 033114 (2010).
16. A. Okubo, *Deep Sea Res. Oceanic Abstr.* **17**, 445.
17. J. Weiss, *Phys. D* **48**, 273 (1991).
18. G. Haller, *Phys. D* **149**, 248 (2001).
19. G. Haller, *Phys. Fluids* **14**, 1851 (2002).
20. G. Haller, *J. Nonlinear Sci.* **10**, 99 (2000).
21. E. Dresselhaus, M. Tabor, *J. Fluid Mech.* **236**, 415 (1992).
22. G. Lapeyre, B. Hua, B. Legras, *J. Nonlinear Sci.* **11**, 427 (2001).
23. T. H. Solomon, I. Mezić, *Nature* **425**, 376 (2003).
24. C. Doering, J. Thiffeault, *Phys. Rev. E Stat. Nonlin. Soft Matter Phys.* **74**, 025301 (2006).
25. S. Plasting, W. Young, *J. Fluid Mech.* **552**, 289 (2006).
26. ftp://satepsanone.nesdis.noaa.gov/OMS/disasters/ DeepwaterHorizon/composites/2010 and www.ssd.noaa. gov/PS/MPS/about.html
27. www.nytimes.com/interactive/2010/05/01/us/20100501-oil-spill-tracker.html
28. We thank B. Lipphardt of the University of Delaware, whose initial calculations showed the potential of the concepts described here in the context of the Gulf oil spill; and G. Haller for useful comments. The work of I.M., S.L., and V.A.F. was supported by Aimdyn. I.M. and S.L. were consultants for Aimdyn. P.H.'s work was supported by the Naval Research Laboratory in Stennis, MS. We are thankful to the leadership of the U.S. Coast Guard at the Cocodrie, Louisiana, site for their interest in this work.

Oscillatory Mass Transport in Vapor-Liquid-Solid Growth of Sapphire Nanowires

Sang Ho Oh,[1,2]* Matthew F. Chisholm,[3] Yaron Kauffmann,[4] Wayne D. Kaplan,[4] Weidong Luo,[3,5] Manfred Rühle,[6] Christina Scheu[7]

In vapor-liquid-solid (VLS) growth, the liquid phase plays a pivotal role in mediating mass transport from the vapor source to the growth front of a nanowire. Such transport often takes place through the liquid phase. However, we observed by in situ transmission electron microscopy a different behavior for self-catalytic VLS growth of sapphire nanowires. The growth occurs in a layer-by-layer fashion and is accomplished by interfacial diffusion of oxygen through the ordered liquid aluminum atoms. Oscillatory growth and dissolution reactions at the top rim of the nanowires occur and supply the oxygen required to grow a new (0006) sapphire layer. A periodic modulation of the VLS triple-junction configuration accompanies these oscillatory reactions.

Vapor-liquid-solid (VLS) growth processes are widely used to grow nanowires composed of functional materials such as semiconductors (1–5), oxides (6, 7), and nitrides (8, 9). Controlled growth of nanowires to a desired size, orientation, morphology, and composition requires understanding of the atomic-level growth mechanism. Relative to established growth processes such as vapor deposition and solidification, less is known about the atomic-scale mechanisms of the reaction steps involved in VLS growth (10–13). Here, we describe the growth mechanism governing self-catalytic VLS growth of (0001) sapphire (α-Al$_2$O$_3$) nanowires, which we observed by in situ high-resolution transmission electron microscopy (HRTEM).

Sapphire nanowires were grown by first forming Al droplets on an α-Al$_2$O$_3$ single crystal by heating the crystal above 660°C in a HRTEM

[1]Department of Materials Science and Engineering, Pohang University of Science and Technology, Pohang 790-784, Korea. [2]National Center for Nanomaterials Technology, Pohang University of Science and Technology, Pohang 790-784, Korea. [3]Materials Science and Technology Division, Oak Ridge National Laboratory, Oak Ridge, TN 37831, USA. [4]Department of Materials Engineering, Technion–Israel Institute of Technology, Haifa 32000, Israel. [5]Department of Physics and Astronomy, Vanderbilt University, Nashville, TN 37235, USA. [6]Max-Planck-Institut für Metallforschung, Heisenbergstr. 3, 70569 Stuttgart, Germany. [7]Department of Chemistry and Center for NanoScience, Ludwig-Maximilians-University, Butenandstr. 11, 81377 Munich, Germany.

*To whom correspondence should be addressed. E-mail: shoh@postech.ac.kr